AGU PUBLICATIONS

JGR

Journal of Geophysical Research: Atmospheres

RESEARCH ARTICLE
10.1002/2016JD025676

Key Points:
- RO_x budget and O_3 production were simulated and studied at Wuhan (urban site) for the first time, central China, using 0-D box model
- Excess HONO contributed up to 31% of O_3 production at this site during the day
- Agricultural biomass burning contributed 18% of O_3 formation during the episode dates

Supporting Information:
- Supporting Information S1

Correspondence to:
Y. Wang and J. C. H. Fung,
yuhang.wang@eas.gatech.edu;
majfung@ust.hk

Citation:
Lu, X., N. Chen, Y. Wang, W. Cao, B. Zhu, T. Yao, J. C. H. Fung, and A. K. H. Lau (2017), Radical budget and ozone chemistry during autumn in the atmosphere of an urban site in central China, *J. Geophys. Res. Atmos.*, *122*, 3672–3685, doi:10.1002/2016JD025676.

Received 20 JUL 2016
Accepted 5 MAR 2017
Accepted article online 8 MAR 2017
Published online 29 MAR 2017

Radical budget and ozone chemistry during autumn in the atmosphere of an urban site in central China

Xingcheng Lu[1], Nan Chen[2], Yuhang Wang[3], Wenxiang Cao[2], Bo Zhu[2], Teng Yao[1], Jimmy C. H. Fung[1,4], and Alexis K. H. Lau[1,5]

[1]Division of Environment, Hong Kong University of Science and Technology, Hong Kong, [2]Hubei Provincial Environmental Monitoring Center, Wuhan, China, [3]School of Earth and Atmospheric Science, Georgia Institute of Technology, Atlanta, Georgia, USA, [4]Department of Mathematics, Hong Kong University of Science and Technology, Hong Kong, [5]Department of Civil and Environmental Engineering, Hong Kong University of Science and Technology, Hong Kong

Abstract The RO_x (=OH + HO_2 + RO_2) budget and O_3 production at an urban site in central China (Wuhan) during autumn were simulated and analyzed for the first time using a UW Chemical Model 0-D box model constrained by in situ observational data. The daytime average OH, HO_2, and RO_2 concentrations were 2.2×10^6, 1.0×10^8, and 5.2×10^7 molecules cm^{-3}, respectively. The average daytime O_3 production rate was 8.8 ppbv h^{-1}, and alkenes were the most important VOC species for O_3 formation (contributing 45%) at this site. Our sensitivity test indicated that the atmospheric environment in Wuhan during autumn belongs to the VOC-limited regime. The daily average HONO concentration at this site during the study period reached 1.1 ppbv and played an important role in the oxidative capacity of the atmosphere. Without the source of excess HONO, the average daytime OH, HO_2, RO_2, and O_3 production rates decreased by 36%, 26%, 27%, and 31% respectively. A correlation between the HONO to NO_2 heterogeneous conversion efficiency and $PM_{2.5}\times$SWR was found at this site; based on this relationship, if the $PM_{2.5}$ concentration met the World Health Organization air quality standard (25 μg m^{-3}), the O_3 production rate in this city would decrease by 19% during late autumn. The burning of agricultural biomass severely affected the air quality in Wuhan during summer and autumn. Agricultural burning was found to account for 18% of the O_3 formation during the study period. Our results suggest that VOC control and a ban on agricultural biomass burning should be considered as high-priority measures for improving the air quality in this region.

1. Introduction

RO_x, composed of OH, HO_2, and organic peroxy (RO_2) radicals, largely controls the oxidation capacity of the atmosphere. Chemical reactions between RO_x and NO_x are central to oxidative processes in the atmospheric environment, which have a substantial effect on air quality via the formation of, for example, O_3 and secondary organic aerosols. Reactive OH and RO radicals are produced by the reactions of HO_2 and RO_2 with NO. At the same time, these two reactions also produce NO_2, a major precursor for the formation of O_3. In both urban and remote areas, the methyl peroxy radical (CH_3O_2) is the dominant RO_2 species, whereas HO_2 concentrations are normally higher than those of RO_2 [*Liu et al.,* 2012; *Xue et al.,* 2013]. The structures and concentrations of the radicals are determined by the nature and abundance of the volatile organic compounds (VOCs) in the atmosphere. All of the radical species (RO_x and NO_x) together with the level of solar radiation determine the O_3 level in the ambient environment.

O_3 is the main component of photochemical smog, one of the most common air pollution events worldwide, especially in China. This pollution is caused by a complicated set of photochemical reactions involving VOCs and NO_x. In the past 10 years, many studies have been made to investigate the RO_x budget and O_3 formation across the country. For example, *Hofzumahaus et al.* [2009] quantified the OH and HO_2 concentrations in the Pearl River Delta (PRD) region and reported an OH concentration (~10^7 molecules cm^{-3}) 3 to 5 times greater than expected. *Lou et al.* [2010] combined observational data and model calculations and found that organic compounds contributed up to 85% of OH reactivity in the PRD region during the afternoon. *Liu et al.* [2012] applied the REAM-1D model to simulate the RO_x budget and O_3 production rate in Beijing. They likewise reported that aromatic compounds, as well as HONO from an unknown source, were the major driving forces for O_3 production in that city. Moreover, some of

the above studies found that the complicated set of photochemical reactions in the atmosphere could not be reconciled with current knowledge. For example, in the case of HONO, great efforts have been devoted to identification of the unknown production sources for this trace gas. *Su et al.* [2011] reported that the unknown HONO may come from soil emissions, and *Liu et al.* [2014] showed that a substantial amount of the unexplained HONO was formed by heterogeneous aerosol reactions by using REAM 1-D model.

Wuhan, the capital city of Hubei province, is one of the most important centers for industry, education, and economy in central China. Concurrently with the "Rise of Central China" strategy, the gross domestic product of this city reached 900 billion Chinese yuan by 2013, placing it in the top 10 Chinese cities. Substantial economic and infrastructural development has brought great benefits to residents, but it has been a "double-edged sword"; urban development has also raised environmental issues for the region, including air pollution and ecological deterioration. The building of a large number of energy-intensive factories and the growth of vehicle ownership have led to substantially increasing emission of SO_2, NO_x, VOC, and primary particulate matter across this region. In addition to these consequences of modernization, the emissions of VOCs and particulate matter from agricultural burning have also exerted adverse effects on the air quality in this region. In the past 10 years, Wuhan has had several severe air pollution issues, including episodes with high levels of O_3 and haze [*X. Lyu et al.*, 2016].

Public consciousness of environmental protection has increased, and several observational and box model-based air quality studies have been carried out in this region. For instance, *Querol et al.* [2006] found that the daily mean PM_{10} concentration reached 156 $\mu g\,m^{-3}$ at residential sites and 197 $\mu g\,m^{-3}$ at industrial sites in the city. Their results also indicated that industrial emissions and power plant combustion were the two major sources of the high PM level in Wuhan. *Xu et al.* [2016] reported that air pollution in Wuhan was associated with urbanization. They found that an area of built-up land was associated with higher SO_2, NO_2, and PM_{10} levels. Recently, *X. P. Lyu et al.* [2016] analyzed the VOC concentration at the same site and reported that coal burning and vehicle exhausts were the two major contributors to O_3 formation there.

Few studies have reported the oxidative capacity, RO_x budget, and O_3 formation in the atmosphere over this region. It is essential to develop a detailed understanding of the ambient RO_x level because it strongly determines the degree of primary pollutant removal and O_3 formation [*Hofzumahaus et al.,* 2009] in the atmosphere. To obtain a full picture of the photochemical reaction processes in Wuhan, we analyzed the RO_x budget and O_3 formation using the observation-constrained UW Chemical Model (UWCM) [*Wolfe and Thornton*, 2011]. This 0-D box model is constrained by physical meteorological parameters (relative humidity, temperature, and pressure) and chemical species, including VOCs, O_3, NO_x, CO, HONO, and HNO_3. Due to the availability and continuity of the relevant VOC data, we chose autumn (26–30 September, 3–6 October, and 26–31 October 2013) for the study period. Sensitivity tests were performed to study the effectiveness of the measures to control O_3 formation at this site. The influence of the excess HONO (HONO from unknown sources other than NO + OH) was also investigated in this study. Agricultural burning is common in autumn across this region. According to the Moderate Resolution Imaging Spectroradiometer near-real-time(MODIS NRT) C5 data product, about 500 fire points were identified across the city in October 2013. Therefore, the effect of biomass burning on O_3 production was also analyzed. The remainder of this paper is organized as follows. Section 2 describes the measurement data and the setup of the UWCM 0-D box model. In section 3.1, we analyze the RO_x budget and its reaction rate. O_3 formation, control strategies for VOCs and NO_x to reduce O_3 production, and the effect of excess HONO on the O_3 budget are presented in section 3.2. Section 3.3 focuses on the effects of biomass burning on O_3 formation in Wuhan. Finally, the overall study is summarized in section 4.

2. Methodology

2.1. Observation Data

During the study period in autumn 2013, a comprehensive set of VOC trace gases, including 48 nonmethane hydrocarbons, 15 halocarbons, and 3 oxygenated VOCs (OVOCs), were measured concurrently at the rooftop (18 m above the ground) of the Hubei Provincial Environmental Monitoring Center (114°21′41″E, 30°31′54″N),

Table 1. Mean Concentrations of Major Organic and Inorganic Gas Species and Meteorological Parameters in Wuhan City During Autumn 2013

	Values
Organic Gases (ppbv)	
Alkanes	
Ethane	4.78
Propane	1.56
Isobutane	1.27
n-Butane	0.97
Isopentane	0.68
n-Pentane	0.86
Cyclopentane	0.22
n-Hexane	0.25
2-Methylpentane	0.27
3-Methylpentane	0.21
Aromatics	
Benzene	2.26
Toluene	1.87
m/p-Xylene	0.40
o-Xylene	0.21
Styrene	0.14
Ethylbenzene	0.52
Alkyne	
Acetylene	2.1
Alkenes	
Ethylene	4.25
Propylene	0.10
trans-2-Butene	0.23
1-Butene	0.31
cis-2-Butene	0.64
1-Pentene	0.10
trans-2-Pentene	0.15
Isoprene	0.05
Inorganic Gases (ppbv)	
NO	11.8
NO_2	32.4
O_3	25.3
CO	1300
HONO	1.1
Meteorological Parameters	
Temperature (K)	292.6
RH	67.4%
Pressure (mbar)	1012.7

in Wuchan district, Wuhan city. The sampling site was located in an urban area, and it was near the traffic lane. A gas chromatograph with a mass spectrometer and flame ionization detector (GC-MS/FID; codeveloped by Wuhan Tianhong Instrument Inc. and Peking University (TH_PKU-300)) was used to measure the real-time VOC levels. After passing through a perfluoroalkoxy Teflon tube, each air sample was purified and concentrated via two steps: (1) a first pass through a temperature of −80°C to remove water vapor and carbon dioxide followed by (2) a second pass through another cold trap at −150°C for concentration. After the purification and concentration processes, the temperature was raised to 100°C and the gas was introduced into the GC-MS/FID system for further measurement. Six different concentrations of a standard sample (0.03–0.25 ppbv) were used to calibrate the GC-MS/FID every 2 weeks. Further details about the detection limits and the quality assurance/quality control of this instrument can be found in *Wang et al.* [2014] and *X. P. Lyu et al.* [2016].

Other trace gases and aerosol components, including HONO, HNO_3, and potassium, were measured online using Measuring AeRosols and GAses (Metrohm-MARGA 1S, Switzerland). The material, diameter, and length of the sample line were linear low-density polyethylene, 1/2″ and 2.5 m, respectively. The flow rate was 16.7 L min^{-1}. The detection limit and repeatability of the HONO measurement were 0.03 μg m^{-3} and 3.3%, respectively. *Nie et al.* [2015] reported that the main source of interference in HONO measurement using MARGA should be mainly from the NO_2 conversion in the wet rotating denuder. We followed their method to correct our HONO data ($HONO_{LOPAP} = 0.833 \times HONO_{WRD} - 0.17$) [*Su*, 2008]. The MARGA system was calibrated each week using a LiBr standard solution to ensure the detection limit and accuracy of the data. The $PM_{2.5}$, SO_2, NO_x, CO, and O_3 levels were measured with a set of related commercial analyzers developed by Thermo Environmental Instruments Inc., USA. $PM_{2.5}$ was measured by a particulate matter detector (Thermo Fisher-1405D), NO_x was detected with a chemiluminescence NO_x analyzer (Model 42i), SO_2 was measured with a fluorescence analyzer (Model 43i), and O_3 and CO were measured with a CO analyzer (Model 48i) and an O_3 analyzer (Model 49i), respectively. The detection limit (precision) for Model 42i, Model 43i, Model 48i, and Model 49i are 0.4 ppbv (±0.4 ppbv), 0.5 ppbv (±1 ppbv), 0.04 ppmv (±0.1 ppmv), and 0.5 ppbv (±1 ppbv), respectively. A molybdenum converter was used for NO_2 measurement, and as a result, part of the NO_y (e.g., peroxyacetylnitrate (PAN), HNO_3, and alkyl nitrates) may have been transformed to NO_2 during the sampling. Therefore, we applied formula (1) in *Lamsal et al.* [2008] to correct our NO_2 data; more detail can be found in the

supporting information. The temporal resolution for the measurement of all of the gases and particulate matter was 1 h. The diurnal profile of NO, NO_2, O_3, and HONO can be found in Figure S1. The average major VOC concentrations can be found in Table 1.

2.2. 0-D Box Model

We used the UWCM 0-D box model to simulate the RO_x budget and O_3 production at this site. This model is a modified version of the UW-CAFE model; further details of this model can be found in *Wolfe and Thornton* [2011] and *Wolfe et al.* [2016]. The organic and inorganic chemistry in this model was based on Master Chemical Mechanisms (MCM) version 3.2 (http://mcm.leeds.ac.uk/MCMv3.2/), a set of near-explicit photooxidation schemes [*Jenkin et al.,* 1997; *Saunders et al.,* 2003]. The gas species identified herein can be described with a total of 10,608 reactions. The UWCM model coupled with MCM has been successfully implemented in other ambient photochemical studies around the world [*Riedel et al.,* 2014; *Kim et al.,* 2015]. The emissions and deposition of chemical species were not considered in the 0-D box model; hence, a 24 h first-order dilution rate scaled by hourly wind speed over daily average wind speed was implemented for all species to prevent those with long lifetimes from increasing to an unrealistic level [*Wolfe et al.,* 2014]. Two days' spin-up was needed, and hence, 8 days of results were available for analysis (29–30 September, 5–6 October, and 28–31 October) [*Kim et al.,* 2015]. Because the photolysis frequencies (*J* values) at this site were not measured during the study period, the National Center for Atmospheric Research tropospheric ultraviolet and visible (TUV) transfer model (http://www.acd.ucar.edu/TUV) was used to calculate the photolysis rate for the box model simulation. The O_3 column density measured by the Total Ozone Mapping Spectrometer, MODIS aerosol optical depth (MYD08), aerosol single scattering albedo (OMAERUVd v003), and Modern Era Retrospective-Analysis for Research and Applications surface albedo (MAT1NXRAD v5.2.0) were used as the inputs for the TUV model. To model the cloud effect, the *J* value (s^{-1}) was scaled with equation (1):

$$J_{\text{corrected}} = J_{\text{TUV}} \times \text{SWR}_{\text{cloud}} / \text{SWR}_{\text{clear}}, \quad (1)$$

where $J_{\text{corrected}}$ represents the scaled photolysis rate, J_{TUV} is the photolysis rate calculated by the TUV model without considering the cloud effect, $\text{SWR}_{\text{cloud}}$ (W m^{-2}) represents the downward short-wave radiation reaching the ground at a specific hour, and $\text{SWR}_{\text{clear}}$ represents the clear-sky downward short-wave radiation at the ground surface. The short-wave radiation reaching the ground was calculated with Weather Research Forecast (WRF) v3.6. The details of the WRF model configuration are introduced in section 2.3. The concentrations of the observed OVOCs (C_2H_5CHO, C_3H_7CHO, and C_4H_9CHO) were compared with those of the OVOCs simulated by the box model without constraints. The daytime average (9:00 to 17:00) observed concentrations of C_2H_5CHO, C_3H_7CHO, and C_4H_9CHO were 1.8, 0.07, and 0.04 ppbv, whereas the daytime average simulated concentrations of these three OVOCs were 1.2, 0.07, and 0.034 ppbv. The concentrations of HCHO and CH_3CHO as simulated by the model were 7.1 and 5.2 ppbv, respectively, which are comparable with the findings of other observational studies in China [*Liu et al.,* 2012; *Zhang et al.,* 2012; *Ma et al.,* 2016]. This comparison indicated that the results simulated by the UWCM 0-D box model could be used for further analysis.

2.3. WRF Model Configuration

We applied the model WRF v3.6 to simulate the wind field and downward short-wave radiation flux. Three nested domains were set, and the domain coverage is shown in Figure S2. Domain 1 (27 km) covered the entire China, as well as some surrounding countries, such as Japan, Korea, Thailand, and most of India. Domain 2 (9 km) covered Hubei, Hunan, Henan, and Jiangxi provinces. Domain 3 (3 km) included all of the cities in Hubei province; the simulation results from this domain were used in the following analysis. We used the Grell-Devenyi ensemble cumulus parameterization scheme [*Grell and Dévényi*, 2002], the Yonsei University planetary boundary layer scheme [*Hong et al.,* 2006], the Morrison two-moment microphysics scheme [*Morrison et al.,* 2009], and the Noah land-surface model [*Chen and Dudhia*, 2001] for the simulation. The scheme of *Dudhia* [1989] was selected for the short-wave radiation, and the Rapid Radiative Transfer Model [*Mlawer et al.,* 1997] was chosen as the long-wave radiation scheme. The short-wave radiation from the WRF model was used to correct the *J* value calculated by the TUV model; the wind direction from the WRF was used to show the observation site was influenced by the surrounding agricultural burning during the late October. A matrix of the performance statistics of WRF is shown in Table S1. In general, the performance of WRF in this study was comparable to that in other study [*Wu et al.,* 2013].

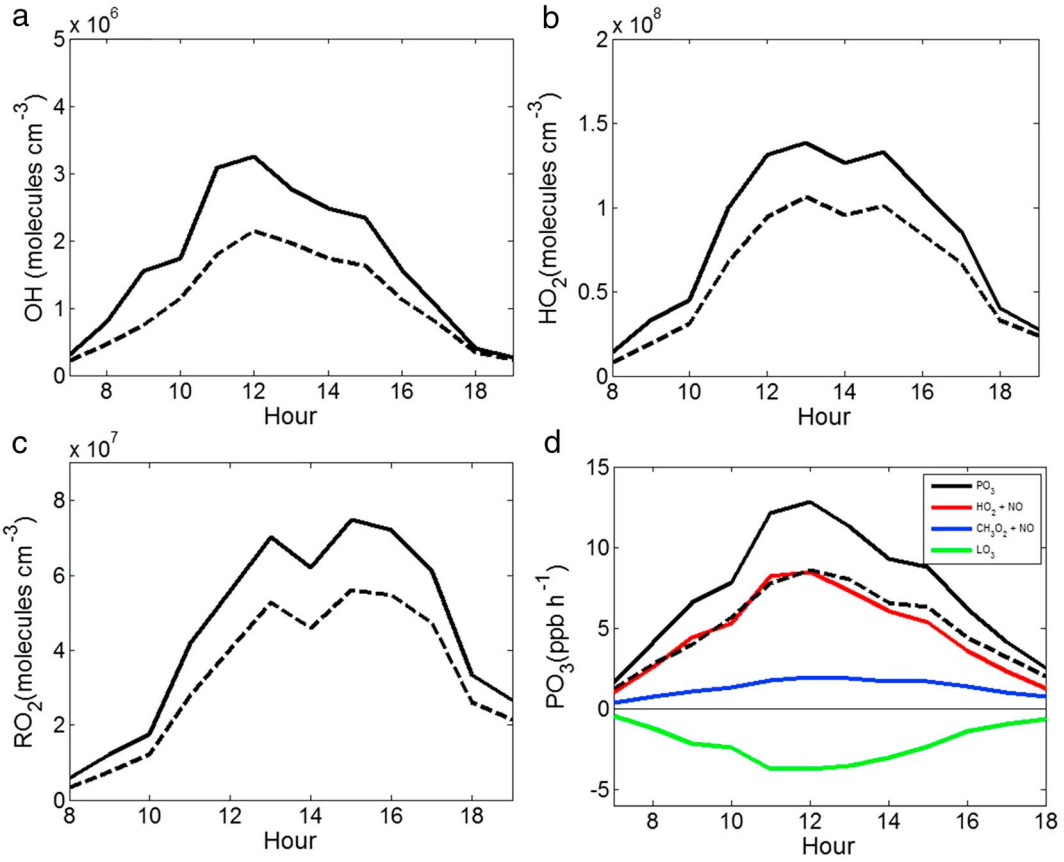

Figure 1. (a–d) Daytime (9:00–17:00) RO_x and O_3 production rates during the study period in Wuhan. Dashed lines represent RO_x concentration/O_3 production rate without constraining the HONO concentration using observational data.

3. Results and Discussions

3.1. RO_x Budget Analysis

As shown in Figures 1a–1c, the 8 day average diurnal highest concentrations of OH, HO_2, and RO_2 reached 3.2×10^6, 1.4×10^8, and 7.0×10^7 molecules cm^{-3} respectively. The peak OH concentration simulated in this study is lower than that in Beijing (9×10^6 molecules cm^{-3}) during August [*Liu et al.,* 2012] and the PRD region (1.3×10^7 molecules cm^{-3}) during July [*Hofzumahaus et al.,* 2009]. However, the simulated OH concentration is higher than that in New York City (1.4×10^6 molecules cm^{-3}) during winter [*Ren et al.,* 2006], Tokyo (1.5×10^6 molecules cm^{-3}) during winter [*Kanaya et al.,* 2007], and the concentration in London (1.8×10^6 molecules cm^{-3}) during July [*Lee et al.,* 2016]. Among the above five studies, the OH concentration reported by *Liu et al.* [2012] was simulated by a 1-D model, while the concentrations in the other four studies were measured by the instruments during field campaigns. The HO_2 concentration simulated in this study is lower than that in Beijing in August (6.8×10^8 molecules cm^{-3}) [*Liu et al.,* 2012] and that in Houston (6.3×10^8 molecules cm^{-3}) during spring [*Ren et al.*, 2013]. However, our simulated result is close to the summer HO_2 concentration in New York City (around 1.25×10^8 molecules cm^{-3}) [*Ren et al.,* 2003] and higher than the observed value in Tokyo (around 3×10^7 molecules cm^{-3}) [*Kanaya et al.,* 2007] during winter. The RO_2 concentration simulated in this work is lower than that in Beijing in August (4.5×10^8 molecules cm^{-3}) [*Liu et al.,* 2012] for two reasons: (1) photolysis rates are generally lower in autumn than summer and (2) the average concentration of aromatics over Beijing (toluene, 5.88 ppbv; ethylbenzene, 3.25 ppbv; and xylene, 5.98 ppbv) during summer is higher than that in Wuhan during autumn. Although the RO_x budget simulated in this study differs from those in other studies, the values (OH peak value: 3.2×10^6; HO_2 peak value: 1.4×10^8; and RO_2 peak value: 7.0×10^7) reported here are on the same magnitude as the observed and simulated values in the studies listed above. Based on those studies, the RO_x concentration is highly dependent on solar radiation, primary OH sources (e.g., HONO), ambient VOC concentration, and NO_x level.

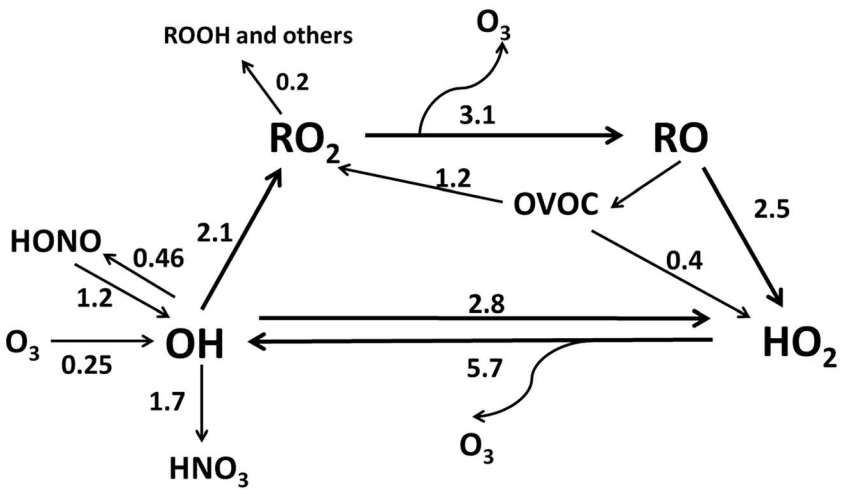

Figure 2. Average reaction rates of RO_x radicals during daytime (9:00–17:00). Units: ppbv h^{-1}.

The dashed line in Figures 1a–1c is the simulated RO_x budget without the source of excess HONO. Specifically, in the dashed line case, the simulated HONO concentration is not constrained in the simulation with observations and there is only one gas-phase production reaction for HONO (NO + OH) in the model. The average HONO concentration produced by NO + OH is only around 0.3 ppbv, whereas the average observed HONO concentration was around 1.1 ppbv during the study period, as shown in Table 1. Such a large discrepancy between the observed and modeled HONO concentrations has a substantial effect on the calculated ambient RO_x budget and oxidative capacity of the atmosphere. As seen in Figures 1a–1c, the 8 day average daytime OH, HO_2, and RO_2 concentrations decreased to some extent without the excess HONO source. In detail, when constrained by the observational data including HONO, the daytime average (9:00–17:00) concentrations of OH, HO_2, and RO_2 were 2.2×10^6, 1.0×10^8, and 5.2×10^7 molecules cm^{-3}, respectively. The daytime average concentrations of these three radicals without the excess HONO source were 1.4×10^6, 7.4×10^7, and 3.8×10^7 molecules cm^{-3}. The OH concentration decreased by 36%, the HO_2 concentration by 26%, and the RO_2 concentration by 27% compared with the HONO-constrained case. Hence, we can conclude that the excess HONO source influences the atmospheric oxidative capacity to a large degree, and the increased level of OH creates a more photochemically active environment in the atmosphere over this region. This excess HONO source was not taken into consideration in some previous model simulations; hence, it is important to include this term in future model-based RO_x budget analysis and studies into O_3 control policy.

The average production and termination rates for the RO_x radical are shown in Figure 2. The reaction $HO_2 + NO$ was the dominant OH formation source, with a reaction rate reaching 5.7 ppbv h^{-1} during the study period. This was followed by the photolysis of HONO; the OH production rate from this reaction was 1.2 ppbv h^{-1}. The major pathways for OH consumption were the formation of HNO_3 and RO_2, with reaction rates of 1.7 and 2.1 ppbv h^{-1} respectively. The high $OH + NO_2$ reaction rate was mainly caused by the relatively high daily average NO_x concentration during the study period, with a value of 44 ppbv. The reaction rate of $HO_2 + NO$ in this study is lower than that reported by *Liu et al.* [2012] (19.8 ppbv h^{-1}, in Beijing) and *Michoud et al.* [2012] (10.9 ppbv h^{-1}, in France). The main reason for this discrepancy is that those two studies were performed during summer, when the photolysis rate is at its highest for the year. The HO_2 formation rates from RO and OVOCs were 2.5 and 0.4 ppbv h^{-1}, respectively. The rate for the transformation of RO to HO_2 is lower than that in Beijing in summer (11 ppbv h^{-1}). The major HO_2 sink was its reduction reaction with NO, which forms OH radicals. Some studies have also found that HO_2 radicals can be absorbed by aerosols [*Thornton and Abbatt*, 2005; *Taketani et al.,* 2012]. *Taketani et al.* [2012] reported that the HO_2 update coefficients at Mount Tai and Mount Mang in China ranged from 0.13 to 0.34 and 0.09 to 0.40, respectively. Aerosol surface area data are not available during our study period, and the HO_2 uptake coefficient has not been studied in this region. Therefore, a future study of the HO_2 heterogeneous uptake coefficient over this region is urgently needed to gain a better understanding of the effect of aerosols on the HO_2 budget. The RO_2

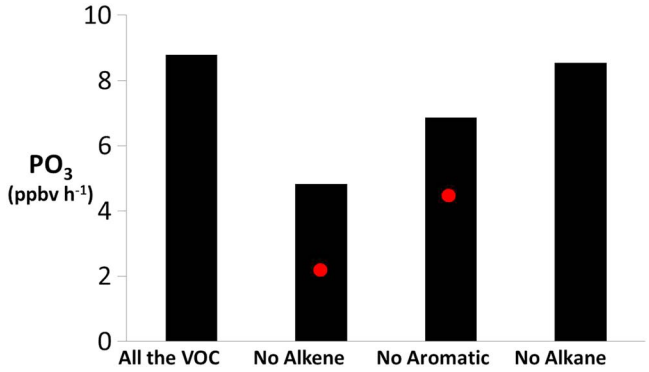

Figure 3. Test of sensitivity of the daytime average O_3 production rate (ppbv h^{-1}) to omission of major VOCs. Red dots represent the O_3 production rate without excess HONO source.

formation rates from OH and OVOCs were 2.1 and 1.2 ppbv h^{-1}, respectively, which are also lower than those reported in summer in Beijing. In addition to the difference in photolysis rates, the ambient VOC concentration is also an important factor that may cause the discrepancy between the RO_2 formation rates in Beijing and Wuhan. As analyzed above, the average ethylbenzene and xylene concentrations in Beijing during the summer of 2007 were 3.25 and 5.98 ppbv, respectively, whereas in our study the concentrations of these two species were only 0.52 and 0.40 ppbv. We also note that due to the high NO_x concentration, the reactions $NO + HO_2$ and $RO_2 + NO$ are the two major pathways for radical cycling at this site, which are commonly seen in NO_x-abundant environments [*Elshorbany et al.,* 2009; *Dusanter et al.,* 2009].

3.2. O_3 Photochemistry Analysis

3.2.1. O_3 Formation

The O_3 production and loss rates are shown in Figure 1d. In general, the ozone gross production rate was defined by the following formula [*Zhang et al.,* 2016]:

$$PO_3 = k_0[NO][HO_2] + \sum_{i=1}^{n} k_i[NO][RO_2]_i, \quad (2)$$

where k_0 is the rate constant for the $NO + HO_2$ reaction, and k_i are the rate constants for each specific $RO_2 + NO$ reaction. The O_3 loss was attributed to the destruction of both NO_2 (e.g., $OH + NO_2$) and O_3 (e.g., $O^1D + H_2O$). During our study period, the O_3 gross production rate reached 8.8 ppb h^{-1}. As expected, the O_3 production rate was highest at noon, with a peak value of 12.8 ppbv h^{-1}. The O_3 loss rate may have been influenced by interference in the NO_2 measurement. The formation of O_3 by the reaction $HO_2 + NO$ was the most important source, with a peak reaction rate of 8.4 ppbv h^{-1} at noon. CH_3O_2 was the most abundant RO_2 species: its contribution to the formation of O_3 peaked at 2.0 ppbv h^{-1} during the study period. The daytime average O_3 loss rate was around 2.6 ppbv h^{-1}, which was lower than the O_3 production rate. Therefore, the average daytime net O_3 production rate at this site was 6.2 ppbv h^{-1} in autumn. Like the RO_x budget, excess HONO plays an important role in O_3 formation. Without the excess HONO, the daytime average O_3 gross formation rate was only 6.1 ppbv h^{-1}, which is around 69% of the original formation rate. From the 0-D box model, we conclude that HONO plays an important role in the formation of O_3. Further research is therefore needed to better understand the HONO formation mechanism and implement it into a 3-D chemical transport model to improve the regional simulation of O_3.

VOCs play a major role in O_3 formation, so we investigated which VOC species contributed most to O_3 production in Wuhan during autumn. We measured the response of the O_3 formation rate to the removal of the three major types of VOC (alkene, alkane, and aromatic) in turn. As shown in Figure 3, the daytime average O_3 production rates in the absence of alkenes, aromatics, and alkanes were 4.8, 6.9, and 8.5 ppbv h^{-1}, respectively. Thus, alkenes are the most important class of VOC species for O_3 formation in Wuhan during autumn. According to Table 1, ethylene was the most abundant alkene species during the study period, while the concentration of isoprene was only 0.05 ppbv due to the sampling site being located in an urban area. Consistent with this finding, *X. P. Lyu et al.* [2016] reported that ethylene had the highest relative incremental reactivity-weighted concentrations among the VOCs at this site in an analysis of the yearly VOC observational data. *Liu et al.* [2012] found that aromatics were the most important VOC species for O_3 formation in summer in Beijing. However, the average total concentration of aromatics in that study (around 18.6 ppbv) was far greater than that measured in this work (around 5.4 ppbv). Although the alkanes had the largest average total concentration in this study (around 11.1 ppbv), this class of VOCs had the least influence on the formation of

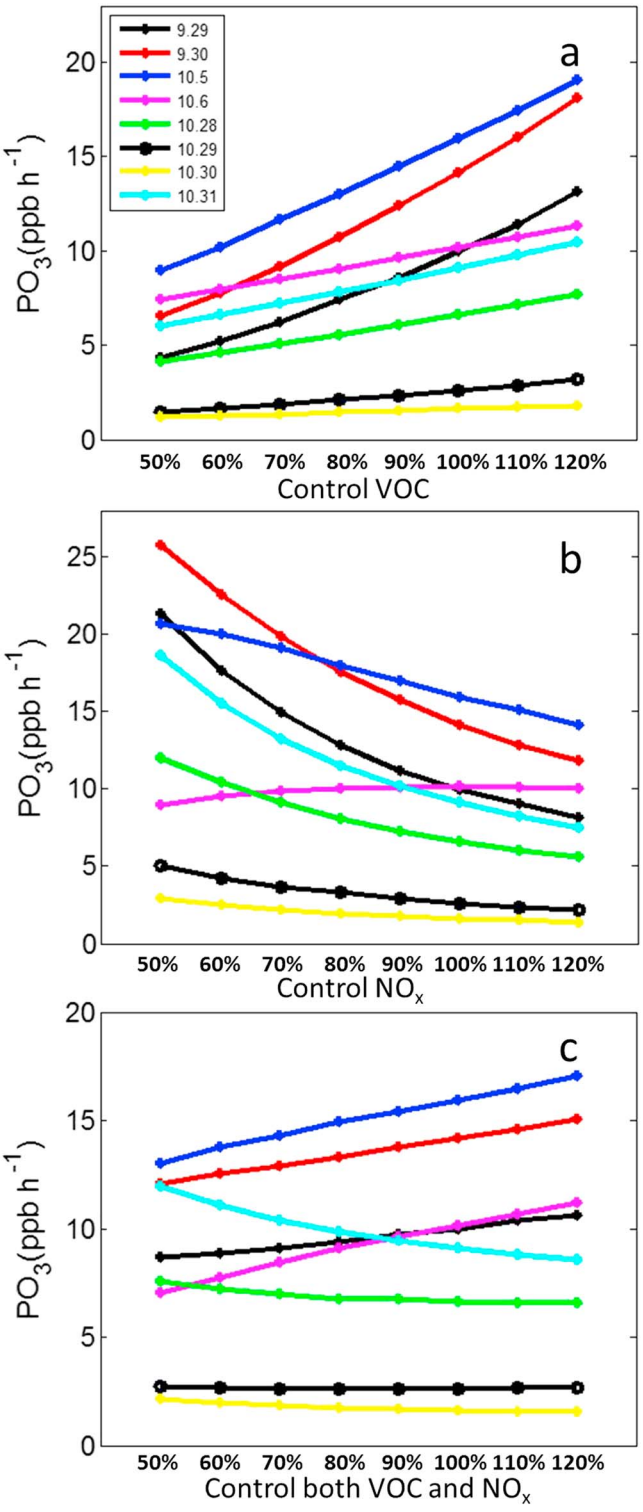

Figure 4. Daily average O_3 production rate under different VOC/NO_x control scenarios. (a) VOC control, (b) NO_x control, and (c) VOC + NO_x control (VOC and NO_x increase or decrease by the same amount). Different colors represent different days in our study period.

O_3, contributing only 2% of the O_3 production, due to their low chemical reactivity. The red dots in Figure 3 represent the O_3 production rates when related VOC species (aromatics or alkene) and excess HONO (HONO from unknown sources other than NO + OH) concentrations were excluded in the model simulation. The O_3 formation rate decreased even further in the absence of excess HONO, falling to just 2.2 and 4.6 ppbv h^{-1} for the alkene and aromatic cases, respectively.

3.2.2. VOC-NO_x Sensitivity Test

Although it is known that alkenes and aromatics are important for O_3 formation at this site during autumn, it is impossible to fully eliminate the emissions of these compounds via an emission control strategy. Scenarios involving changes of 50% to 120% in the emissions of VOC, NO_x, and VOC + NO_x were simulated to study the response of the O_3 production rate to the corresponding emission control strategy. As shown in Figure 4, when the concentration of VOCs was reduced on all 8 days of the study period, the O_3 production rate for each day decreased by an amount proportional to the VOC reduction. Therefore, the ambient environment is classified as a VOC-limited regime during our study period at this site. The O_3 production rate increased as NO_x was reduced on 7 of the 8 days. The response of O_3 production to the primary pollutants (e.g., NO_x and VOC) was not linear. There were notable day-to-day variations in the responses to the combined reduction of VOC and NO_x. For instance, the O_3 production rate increased on 28 and 31 October but decreased on 28 September and 5 October at the same site, under the combined control of VOC + NO_x.

Table 2 shows the 8 day average daytime O_3 production rates under different control scenarios. The O_3 production rate decreased gradually from 8.8 to 5.0 ppbv h^{-1} when VOC emissions were reduced from 100% to 50%. The O_3 production rate increased to 14.4 ppbv h^{-1} when the NO_x emissions

Table 2. Daytime Average O_3 Production Rate (ppbv h^{-1}) Under Different VOC and NO_x Control Scenarios

	VOC	NO_x	VOC + NO_x
120%	10.6	7.7	9.2
110%	9.6	8.1	9.0
100%	8.8	8.8	8.8
90%	7.9	9.5	8.6
80%	7.1	10.4	8.5
70%	6.4	11.5	8.3
60%	5.7	12.8	8.2
50%	5.0	14.4	8.2

were decreased by 50%. The O_3 formation rate was mostly unresponsive to the combined control of VOC and NO_x and was only slightly reduced to 8.2 ppbv h^{-1} when both VOCs and NO_x were reduced by 50%. Our sampling site was around 20 m away from the nearest road which was thus exposed to relatively high levels of NO_x. Due to the likely heterogeneity of pollutants concentration, the O_3 production rate for some urban locations that are farther from a road or nearer to industries with high VOC emissions may be different from this study. The ratio of VOCs to NO_x may also be different in rural area in Hubei province. Further analysis of other sites surrounding the city is urgently needed to devise a suitable air pollution control policy for the entire Hubei region.

3.2.3. Effect of Aerosols on O_3 Formation

As described in the previous section, in addition to HONO production from NO + OH, an excess source of HONO exists in the ambient environment. Several mechanisms for the formation of excess HONO involving the conversion of NO_2 or HNO_3 at ground level and in forests have been proposed [*Zhou et al.,* 2011; *Wong et al.,* 2013]. However, some studies have proposed that the excess HONO source may be the heterogeneous transformation of NO_2 on aerosol surfaces. *Yu et al.* [2009] found that high soot loading was responsible for the high HONO concentration in Nepal. *Liu et al.* [2014] combined observational data, a 1-D model, and a 3-D chemical transport model to demonstrate that the heterogeneous reaction of NO_2 on aerosol surfaces was the major daytime HONO source in Beijing. *Hou et al*. [2016] reported that the HONO excess increased substantially during severe haze in Beijing and that the HONO concentration was closely correlated with the $PM_{2.5}$ mass concentration. All of these studies provide evidence that aerosols may be associated with the major excess HONO source.

In this work, the excess HONO production rate from NO_2 molecule was calculated by ($J[HONO]_{obs} + k_1 \times [HONO] \times [OH] - k_2 \times [NO] \times [OH]$) divided by the NO_2 concentration. The calculated production rate may have been influenced by the NO_2 measurement interference (e.g., PAN) and the chosen correction method. As discussed above, unknown HONO may be formed by reactions on aerosol surfaces or the ground surface; however, it is difficult to determine the relative contributions from these two sources. As presented in Figure S3 (supporting information), the coefficient R^2 between $PM_{2.5} \times SWR$ and the excess HONO production rate normalized by NO_2 during our study period reached 0.38, indicating that part of the excess HONO at this site likely arose from the transformation of NO_2 on aerosol surfaces. The heterogeneous formation of HONO at this site was also likely enhanced by photolysis because the R^2 between $PM_{2.5}$ and the excess HONO production rate was only 0.1. According to World Health Organization (WHO) guidance, the maximum acceptable 24 h $PM_{2.5}$ concentration is 25 $\mu g\,m^{-3}$ [*World Health Organization*, 2006]. To study the effect of aerosols on the photochemistry at this site, the $PM_{2.5} \times SWR$ was reduced by a factor of [$PM_{2.5}$_obs/25 $\mu g\,m^{-3}$] and new excess HONO production rate was calculated by the relationship in Figure S3. Using this method, the time series trend was held constant, and the mean daily $PM_{2.5}$ concentration was converted to 25 $\mu g\,m^{-3}$, the WHO air quality threshold. The HONO from NO + OH was then added back to the new excess HONO term, and the model was constrained by this new HONO concentration in the simulation of sensitivity to aerosols. The average $PM_{2.5}$ concentration on 5 days (5, 6, and 28–30) in October was over 90 $\mu g\,m^{-3}$ (no aerosol data were available for 31 October). The sensitivity to aerosols was therefore simulated on these 5 days. We cannot exclude the possibility that the excess HONO source may be ground-surface heterogeneous conversion of NO_2, photolysis of deposited nitrate, soil emission, or tailpipe emissions. The effects of different forms of land use on the heterogeneous conversion of NO_2 to HONO are still unclear. *VandenBoer et al.* [2015] reported that acid displacement could contribute to daytime HONO emissions in urban areas but were unable to precisely quantify this effect. It is also possible that part of the HONO arises from vehicle emissions at this site [*Kirchstetter et al.,* 1996]. Hence, further studies of the HONO formation mechanism are needed to better understand the urban HONO budget.

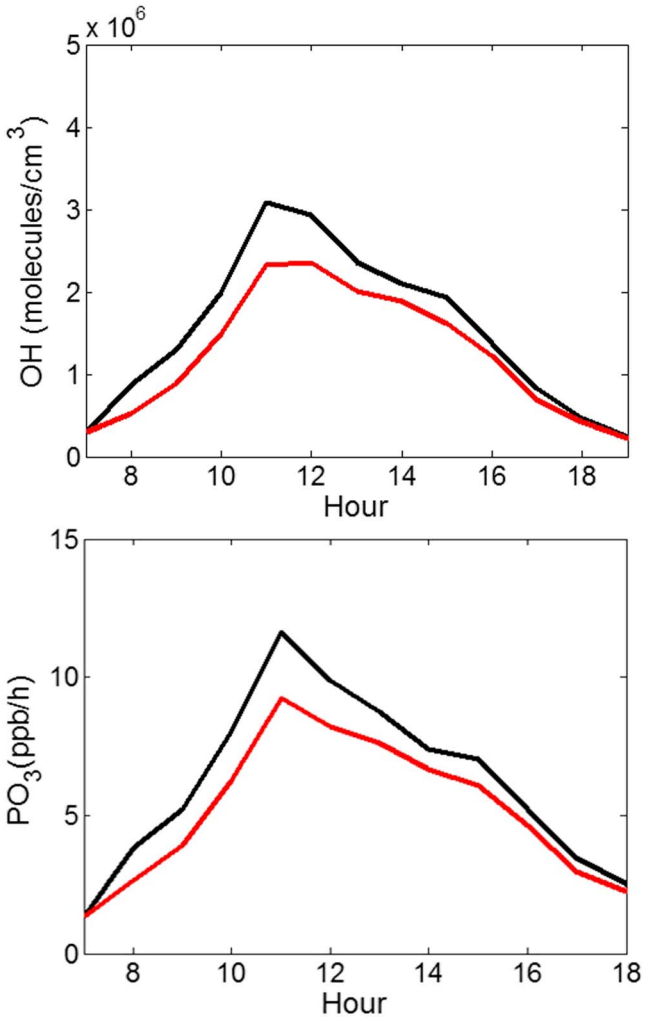

Figure 5. OH radical concentration and O_3 formation under the standard scenario (black line) and $PM_{2.5}$ reduction scenario (red line).

When the $PM_{2.5}$ mass concentration was constrained to meet the WHO air quality standard, during the 5 days in October listed above, the daytime average OH radical concentration decreased from 2.0×10^6 to 1.6×10^6 molecules cm^{-3} (−24%), the HO_2 concentration decreased from 1.36×10^8 to 1.1×10^8 molecules cm^{-3} (−19%), the RO_2 concentration decreased from 7×10^7 to 5.6×10^7 molecules cm^{-3} (−19%), and the O_3 production rate decreased from 7.4 to 6.2 ppbv h^{-1} (−16%). Figure 5 shows the daytime production of O_3 and OH after adjusting the $PM_{2.5}$ concentration to 25 μg m^{-3}. Hence, our results indicate that reducing the aerosol concentration could help to reduce O_3 formation at this site. Combined with the results in section 3.2.2, the optimum air quality improvement strategy at this site would be the joint reduction of VOCs and aerosols. However, because part of the unknown HONO may come from ground heterogeneous transformation of NO_2, therefore, the actual effect of aerosol may be lower than our calculated value.

Aerosols can also reflect or absorb radiation in the atmosphere, and the aerosol optical depth (AOD) is a parameter used to characterize the extinction of solar radiation by aerosols. Some studies have shown that aerosols can influence O_3 formation by attenuating downward short-wave radiation. For example, using a 3-D chemical transport model, *Li et al.* [2011] reported that the photolysis frequency decreased as the AOD increased. *Bian et al.* [2007] found that the O_3 concentration was sensitive to aerosol loading in Tianjing, China. In our study, no hourly AOD was available, so we could not characterize a direct relationship between the hourly AOD and the surface $PM_{2.5}$ concentration at the study site. However, we carried out a sensitivity test of the effect of AOD on the O_3 production rate by using fixed AOD values. The O_3 formation rates were 12.2, 11.1, 10.1, 9.3, 8.6, and 7.9 ppbv h^{-1} when the AOD was fixed at 0, 0.2, 0.4, 0.6, 0.8, and 1.0 in the TUV model, respectively. This result indicates that as the aerosol loading increases, the O_3 production rate decreases, in contrast to the effect of aerosols on HONO formation. The O_3 production rate was also influenced by the single-scattering albedo (SSA) of the aerosol. The O_3 production rate became 6.8 ppbv h^{-1}, 7.3 ppbv h^{-1}, 8.2 ppbv h^{-1}, 9.0 ppbv h^{-1} and 10.1 ppbv h^{-1} when we set the SSA to 0.8, 0.85, 0.9, 0.95, and 1.0 respectively. Observations of the photolysis rates and $PM_{2.5}$ will be needed to quantify this effect.

The effects of aerosol uptake on HO_2 radicals were not considered in this study because no data were available on the aerosol surface area. If this mechanism was active, the HO_2 concentration would decrease as the aerosol concentration increased, and the O_3 formation rate from the reaction $HO_2 + NO$ would decrease in turn. Therefore, in future studies, it will be necessary to measure the aerosol uptake coefficient

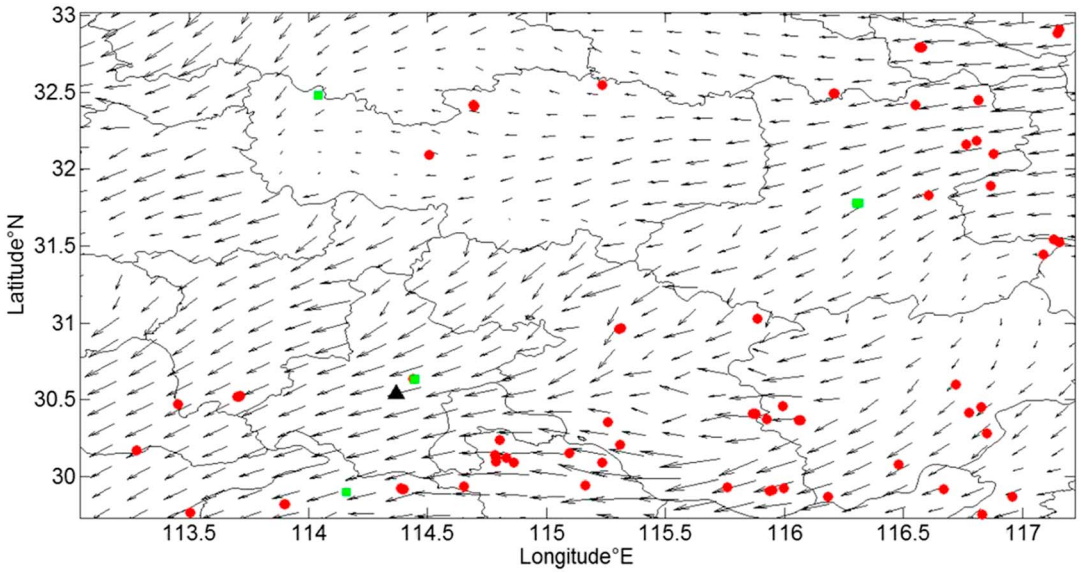

Figure 6. Map of fire points (by MODIS) and wind direction. The triangle represents our study site, red dots represent fire points between 25 and Oct 30 October, and green squares represent fire points between 25 and 30 September.

for HO_2 in this region and to analyze the combined effect of aerosols on HONO, AOD, and HO_2 and the consequences for O_3 formation.

3.3. Agricultural Burning Effect

Surrounded by a large area of farming land, Wuhan is heavily affected by the agricultural burning of biomass in its rural environs. Based on the MODIS NRT C5 fire data (https://firms.modaps.eosdis.nasa.gov/firemap/), more than 500 fire hot spots were detected in Hubei province during October 2013. Agricultural burning emits substantial amounts of VOCs, CO, and aerosols, which can increase the ambient concentrations of those pollutants in urban areas. Hence, it is important to understand how such activity influences O_3 formation at our study site.

Figure 6 presents the fire points (by MODIS) and wind direction simulated by WRF. The average simulated wind direction is that during the period 28–30 October (average of the first 10 layers, approximately 300 m above ground). There were only four fire points between 25 and 30 September (green squares), so this period was not influenced by agricultural burning. However, between 25 and 30 October, more than 50 fire points were detected in the area surrounding our study site, from which we can infer that the site was influenced by agricultural burning during this period. *Nie et al.* [2015] used the concentration of K^+ (an aerosol component) to classify the agricultural burning plume: if $K^+ > 2\,\mu g\,m^{-3}$ and $K^+/PM_{2.5} > 0.02$, then it is highly likely that the ambient environment is influenced by agricultural burning. None of the data met this requirement between and 30 September 28, whereas from 28 to 30 October, almost all of the data met this requirement, excluding only 3-hourly measurements. The acetonitrile (CH_3CN) concentration also proved to be a good indicator of the agricultural burning effect. Between 28 and 30 September, the acetonitrile concentration was around 0.4 ppbv, while from 28 to 30 October, the concentration of this species reached up to 2.69 ppbv. In addition to potassium and acetonitrile, the average concentrations of $PM_{2.5}$, CO, C_2H_2, and C_2H_4 from 28 to 30 October were all higher than those from 28 to 30 September. Hence, it can be confirmed that 28 to 30 October was influenced by biomass burning, whereas no such effect was present from 28 to 30 September.

Yuan et al. [2010] and *Jost et al.* [2003] showed that the effect of agricultural burning on the ambient environment can be quantified by the relationship between VOCs and acetonitrile. Hence, we substituted the background concentration of acetonitrile (the average concentration from 28 to 30 September) into the relationship between acetonitrile and specific gas species to acquire the VOC and CO concentrations in the absence of the biomass burning effect between 28 and 30 October. The relationships between acetonitrile and carbon monoxide, toluene, benzene, ethylbenzene, acetylene, and ethylene are shown in Figure S3.

The correlation coefficient (R^2) between acetonitrile and almost all of these species exceeded 0.25 during our study period (except o-xylene). To simulate the PO_3 without the biomass burning effect, the acetonitrile level measured between 28 and 30 September (0.4 ppbv) was used as a background and the VOC levels were scaled to this acetonitrile background level using the correlation in Figure S4.

The simulated O_3 production rate in original run between 28 and 30 October was 3.6 ppbv h^{-1}. When the extra VOCs and CO from agricultural burning were removed, the O_3 production rate decreased to 2.9 ppbv h^{-1} (−18%). Note that the agricultural burning is very frequent in Hubei province during the summer. For example, according to the MODIS NRT C5 fire data, more than 1300 fire hot spots were detected from June to August 2013. At this site, agricultural burning can be expected to play a particularly important role in O_3 formation during summer due to the higher photolysis rate. *Yamaji et al.* [2010] and *Pan et al.* [2015] also reported that biomass burning is detrimental to the air quality in central China. Therefore, the local government would be advised to restrict agricultural burning in this region to reduce the local O_3 concentration. The original simulated O_3 formation rate between 28 and 30 October was lower than the 8 day average. The 29 and 30 October study periods were cloudy days, so the *J* values for these 2 days were heavily scaled down (see equation (1) and section 2.2). The high VOC concentrations on 28–30 October may have been partly caused by anthropogenic emissions. In the future, simulations using a 3-D chemical transport model, which can rule out the contribution from local emissions, will be needed to further study the exact effect of biomass burning on the air quality in this region.

4. Conclusions

The UWCM 0-D box model involving MCM v3.2 chemical mechanism was combined with observational data to analyze the RO_x budget and O_3 production rate in the city of Wuhan during autumn. Our results showed that the average maximum concentrations of OH, HO_2, and RO_2 were 3.2×10^6, 1.4×10^8, and 7.0×10^7 molecules cm^{-3}, respectively, of the same order of magnitude as in other regions (Beijing, New York, Tokyo, and London). The reaction $HO_2 + NO$ was the major OH production source, with an average reaction rate of 5.7 ppbv h^{-1} during the study period. The daytime average O_3 formation rate was 8.8 ppbv h^{-1}, and the loss rate was 2.6 ppbv h^{-1}. Unlike in Beijing in summer, alkenes contributed the most to O_3 formation in Wuhan during autumn, accounting for 45% of O_3 production in this study. VOC/NO_x sensitivity tests indicated that the ambient environment belonged to the VOC-limited regime during the study period. In general, a 50% decrease in the VOC concentration was found to reduce the O_3 production rate from 8.8 to 5.0 ppbv h^{-1}, whereas the equivalent reduction for NO_x would increase the O_3 production rate from 8.8 to 14.4 ppbv h^{-1}. The O_3 formation rate did not change greatly when both VOCs and NO_x were controlled together. Our results also show that aerosols promoted HONO formation and, as a result, O_3 production. If the ambient $PM_{2.5}$ concentration were decreased to 25 μg m^{-3} (the WHO standard), the O_3 formation rate would fall from 7.4 to 6.0 ppbv h^{-1} (−19%). Therefore, from a control policy perspective, we would advise local government to prioritize their efforts to reduce both the ambient VOC and $PM_{2.5}$ concentrations. Our results also show that biomass burning contributed around 18% of O_3 formation at this site during agricultural burning episodes. Hence, to further minimize the O_3 concentration in this city, the government should also monitor and restrict agricultural burning in the region. This study is only valid for the Wuhan urban area. O_3 is a secondary ambient pollutant, and a substantial amount of it in the urban area may originate from upwind of the city. To establish a control policy for the entire region, further study of the area surrounding this city is needed.

Acknowledgments

We thank Glenn Wolfe who distributed the UWCM box model source code to the public. We also thank the two anonymous reviewers for their constructive comments. Xingcheng Lu was supported by the Overseas Research Award from the Hong Kong University of Science and Technology. Yuhang Wang is supported by the Atmospheric Chemistry Program of the U.S. National Science Foundation. This research was also support by Hong Kong RGC funding (project C5022-14G). The MODIS NRT C5 data product can be found at https://firms.modaps.eosdis.nasa.gov/firemap/. The AOD and SSA data can be downloaded via https://giovanni.sci.gsfc.nasa.gov/giovanni/. The chemical species data used in this study are available from J.C.H Fung (majfung@ust.hk).

References

Bian, H., S. Han, X. Tie, M. Sun, and A. Liu (2007), Evidence of impact of aerosols on surface ozone concentration in Tianjin, China, *Atmos. Environ.*, *41*(22), 4672–4681.

Chen, F., and J. Dudhia (2001), Coupling an advanced land surface-hydrology model with the Penn State-NCAR MM5 modeling system. Part I: Model implementation and sensitivity, *Mon. Weather Rev.*, *129*(4), 569–585.

Dudhia, J. (1989), Numerical study of convection observed during the winter monsoon experiment using a mesoscale two-dimensional model, *J. Atmos. Sci.*, *46*(20), 3077–3107.

Dusanter, S., D. Vimal, P. S. Stevens, R. Volkamer, and L. T. Molina (2009), Measurements of OH and HO_2 concentrations during the MCMA-2006 field campaign—Part 1: Deployment of the Indiana University laser-induced fluorescence instrument, *Atmos. Chem. Phys.*, *9*(5), 1665–1685.

Elshorbany, Y. F., R. Kurtenbach, P. Wiesen, E. Lissi, M. Rubio, G. Villena, E. Gramsch, A. R. Rickard, M. J. Pilling, and J. Kleffmann (2009), Oxidation capacity of the city air of Santiago, Chile, *Atmos. Chem. Phys.*, *9*(6), 2257–2273.

Grell, G. A., and D. Dévényi (2002), A generalized approach to parameterizing convection combining ensemble and data assimilation techniques, *Geophys. Res. Lett.*, *29*(14), 1693, doi:10.1029/2002GL015311.

Hofzumahaus, A., et al. (2009), Amplified trace gas removal in the troposphere, *Science*, *324*(5935), 1702–1704.

Hong, S. Y., Y. Noh, and J. Dudhia (2006), A new vertical diffusion package with an explicit treatment of entrainment processes, *Mon. Weather Rev.*, *134*(9), 2318–2341.

Hou, S., S. Tong, M. Ge, and J. An (2016), Comparison of atmospheric nitrous acid during severe haze and clean periods in Beijing, China, *Atmos. Environ.*, *124*, 199–206.

Jenkin, M. E., S. M. Saunders, and M. J. Pilling (1997), The tropospheric degradation of volatile organic compounds: A protocol for mechanism development, *Atmos. Environ.*, *31*(1), 81–104.

Jost, C., J. Trentmann, D. Sprung, M. O. Andreae, J. B. McQuaid, and H. Barjat (2003), Trace gas chemistry in a young biomass burning plume over Namibia: Observations and model simulations, *J. Geophys. Res.*, *108*(D13), 8482, doi:10.1029/2002JD002431.

Kanaya, Y., R. Cao, H. Akimoto, M. Fukuda, Y. Komazaki, Y. Yokouchi, M. Koike, H. Tanimoto, N. Takegawa, and Y. Kondo (2007), Urban photochemistry in central Tokyo: 1. Observed and modeled OH and HO_2 radical concentrations during the winter and summer of 2004, *J. Geophys. Res.*, *112*, D21312, doi:10.1029/2007JD008670.

Kim, S., S. Y. Kim, M. Lee, H. Shim, G. M. Wolfe, A. B. Guenther, A. He, Y. Hong, and J. Han (2015), Impact of isoprene and HONO chemistry on ozone and OVOC formation in a semirural South Korean forest, *Atmos. Chem. Phys.*, *15*(8), 4357–4371.

Kirchstetter, T. W., R. A. Harley, and D. Littlejohn (1996), Measurement of nitrous acid in motor vehicle exhaust, *Environ. Sci. Technol.*, *30*(9), 2843–2849.

Lamsal, L. N., R. V. Martin, A. Van Donkelaar, M. Steinbacher, E. A. Celarier, E. Bucsela, E. J. Dunlea, and J. P. Pinto (2008), Ground-level nitrogen dioxide concentrations inferred from the satellite-borne Ozone Monitoring Instrument, *J. Geophys. Res.*, *113*, D16308, doi:10.1029/2007JD009235.

Lee, J. D., L. K. Whalley, D. E. Heard, D. Stone, R. E. Dunmore, J. F. Hamilton, D. E. Young, J. D. Allan, S. Laufs, and J. Kleffmann (2016), Detailed budget analysis of HONO in central London reveals a missing daytime source, *Atmos. Chem. Phys.*, *16*(5), 2747–2764.

Li, J., et al. (2011), Impacts of aerosols on summertime tropospheric photolysis frequencies and photochemistry over Central Eastern China, *Atmos. Environ.*, *45*(10), 1817–1829.

Liu, Z., et al. (2012), Summertime photochemistry during CAREBeijing-2007: RO_x budgets and O_3 formation, *Atmos. Chem. Phys.*, *12*(16), 7737–7752.

Liu, Z., Y. Wang, F. Costabile, A. Amoroso, C. Zhao, L. G. Huey, R. Stickel, J. Liao, and T. Zhu (2014), Evidence of aerosols as a media for rapid daytime HONO production over China, *Environ. Sci. Technol.*, *48*(24), 14,386–14,391.

Lou, S., et al. (2010), Atmospheric OH reactivities in the Pearl River Delta–China in summer 2006: Measurement and model results, *Atmos. Chem. Phys.*, *10*(22), 11,243–11,260.

Lyu, X., N. Chen, H. Guo, L. Zeng, W. Zhang, F. Shen, J. Quan, and N. Wang (2016), Chemical characteristics and causes of airborne particulate pollution in warm seasons in Wuhan, central China, *Atmos. Chem. Phys.*, *16*(16), 10,671–10,687.

Lyu, X. P., N. Chen, H. Guo, W. H. Zhang, N. Wang, Y. Wang, and M. Liu (2016), Ambient volatile organic compounds and their effect on ozone production in Wuhan, central China, *Sci. Total Environ.*, *541*, 200–209.

Ma, Y., Y. Diao, B. Zhang, W. Wang, X. Ren, D. Yang, M. Wang, X. Shi, and J. Zheng (2016), Detection of formaldehyde emissions from an industrial zone in the Yangtze River Delta region of China using a proton transfer reaction ion-drift chemical ionization mass spectrometer, *Atmos. Meas. Tech.*, *9*(12), 6101.

Michoud, V., et al. (2012), Radical budget analysis in a suburban European site during the MEGAPOLI summer field campaign, *Atmos. Chem. Phys.*, *12*(24), 11,951–11,974.

Mlawer, E. J., S. J. Taubman, P. D. Brown, M. J. Iacono, and S. A. Clough (1997), Radiative transfer for inhomogeneous atmospheres: RRTM, a validated correlated-k model for the longwave, *J. Geophys. Res.*, *102*(D14), 16,663–16,682, doi:10.1029/97JD00237.

Morrison, H., G. Thompson, and V. Tatarskii (2009), Impact of cloud microphysics on the development of trailing stratiform precipitation in a simulated squall line: Comparison of one-and two-moment schemes, *Mon. Weather Rev.*, *137*(3), 991–1007.

Nie, W., et al. (2015), Influence of biomass burning plumes on HONO chemistry in eastern China, *Atmos. Chem. Phys.*, *15*(3), 1147–1159.

Pan, X., Y. Kanaya, H. Tanimoto, S. Inomata, Z. Wang, S. Kudo, and I. Uno (2015), Examining the major contributors of ozone pollution in a rural area of the Yangtze River Delta region during harvest season, *Atmos. Chem. Phys.*, *15*(11), 6101–6111.

Querol, X., X. Zhuang, A. Alastuey, M. Viana, W. Lv, Y. Wang, A. López, Z. Zhu, H. Wei, and S. Xu (2006), Speciation and sources of atmospheric aerosols in a highly industrialised emerging mega-city in central China, *J. Environ. Monit.*, *8*(10), 1049–1059.

Ren, X., et al. (2003), OH and HO_2 chemistry in the urban atmosphere of New York City, *Atmos. Environ.*, *37*(26), 3639–3651.

Ren, X., et al. (2006), Behavior of OH and HO_2 in the winter atmosphere in New York City, *Atmos. Environ.*, *40*, 252–263.

Ren, X., et al. (2013), Atmospheric oxidation chemistry and ozone production: Results from SHARP 2009 in Houston, Texas, *J. Geophys. Res. Atmos.*, *118*, 5770–5780.

Riedel, T. P., et al. (2014), An MCM modeling study of nitryl chloride ($ClNO_2$) impacts on oxidation, ozone production and nitrogen oxide partitioning in polluted continental outflow, *Atmos. Chem. Phys.*, *14*(8), 3789–3800.

Saunders, S. M., M. E. Jenkin, R. G. Derwent, and M. J. Pilling (2003), Protocol for the development of the Master Chemical Mechanism, MCM v3 (Part A): tropospheric degradation of non-aromatic volatile organic compounds, *Atmos. Chem. Phys.*, *3*(1), 161–180.

Su, H. (2008), HONO: a study to its sources and impacts from field measurements at the sub-urban areas of PRD region, PhD thesis, Peking Univ.

Su, H., Y. Cheng, R. Oswald, T. Behrendt, I. Trebs, F. X. Meixner, M. O. Andreae, P. Cheng, Y. Zhang, and U. Pöschl (2011), Soil nitrite as a source of atmospheric HONO and OH radicals, *Science*, *333*(6049), 1616–1618.

Taketani, F., Y. Kanaya, P. Pochanart, Y. Liu, J. Li, K. Okuzawa, K. Kawamura, Z. Wang, and H. Akimoto (2012), Measurement of overall uptake coefficients for HO_2 radicals by aerosol particles sampled from ambient air at Mts. Tai and Mang (China), *Atmos. Chem. Phys.*, *12*(24), 11,907–11,916.

Thornton, J., and J. P. Abbatt (2005), Measurements of HO_2 uptake to aqueous aerosol: Mass accommodation coefficients and net reactive loss, *J. Geophys. Res.*, *110*, D08309, doi:10.1029/2004JD005402.

VandenBoer, T. C., C. J. Young, R. K. Talukdar, M. Z. Markovic, S. S. Brown, J. M. Roberts, and J. G. Murphy (2015), Nocturnal loss and daytime source of nitrous acid through reactive uptake and displacement, *Nat. Geosci.*, *8*(1), 55–60.

Wang, H., et al. (2014), Source profiles of volatile organic compounds from biomass burning in Yangtze River Delta, China, *Aerosol Air Qual. Res.*, *14*(3), 818–828.

Wolfe, G. M., and J. A. Thornton (2011), The Chemistry of Atmosphere-Forest Exchange (CAFE) Model—Part 1: Model description and characterization, *Atmos. Chem. Phys.*, *11*(1), 77–101.
Wolfe, G. M., et al. (2014), Missing peroxy radical sources within a summertime ponderosa pine forest, *Atmos. Chem. Phys.*, *14*(9), 4715–4732.
Wolfe, G. M., M. R. Marvin, S. J. Roberts, K. R. Travis, and J. Liao (2016), The Framework for 0-D Atmospheric Modeling (F0AM) v3. 1, *Geosci. Model Dev.*, *9*(9), 3309.
Wong, K. W., C. Tsai, B. Lefer, N. Grossberg, and J. Stutz (2013), Modeling of daytime HONO vertical gradients during SHARP 2009, *Atmos. Chem. Phys.*, *13*(7), 3587–3601.
World Health Organization (2006), *Air Quality Guidelines: Global Update 2005: Particulate Matter, Ozone, Nitrogen Dioxide, and Sulfur Dioxide*, World Health Organ., Copenhagen.
Wu, D., J. C. H. Fung, T. Yao, and A. K. H. Lau (2013), A study of control policy in the Pearl River Delta region by using the particulate matter source apportionment method, *Atmos. Environ.*, *76*, 147–161.
Xu, G., L. Jiao, S. Zhao, M. Yuan, X. Li, Y. Han, B. Zhang, and T. Dong (2016), Examining the impacts of land use on air quality from a spatio-temporal perspective in Wuhan, China, *Atmosphere*, *7*(5), 62.
Xue, L. K., T. Wang, H. Guo, D. R. Blake, J. Tang, X. C. Zhang, S. M. Saunders, and W. X. Wang (2013), Sources and photochemistry of volatile organic compounds in the remote atmosphere of western China: Results from the Mt. Waliguan Observatory, *Atmos. Chem. Phys.*, *13*(17), 8551–8567.
Yamaji, K., et al. (2010), Impact of open crop residual burning on air quality over central eastern China during the Mount Tai Experiment 2006 (MTX2006), *Atmos. Chem. Phys.*, *10*(15), 7353–7368.
Yu, Y., B. Galle, A. Panday, E. Hodson, R. Prinn, and S. Wang (2009), Observations of high rates of NO_2-HONO conversion in the nocturnal atmospheric boundary layer in Kathmandu, Nepal, *Atmos. Chem. Phys.*, *9*(17), 6401–6415.
Yuan, B., Y. Liu, M. Shao, S. Lu, and D. G. Streets (2010), Biomass burning contributions to ambient VOCs species at a receptor site in the Pearl River Delta (PRD), China, *Environ. Sci. Technol.*, *44*(12), 4577–4582.
Zhang, Y., Y. Mu, J. Liu, and A. Mellouki (2012), Levels, sources and health risks of carbonyls and BTEX in the ambient air of Beijing, China, *J. Environ. Sci.*, *24*(1), 124–130.
Zhang, Y., et al. (2016), Large vertical gradient of reactive nitrogen oxides in the boundary layer: Modeling analysis of DISCOVER-AQ 2011 observations, *J. Geophys. Res. Atmos.*, *121*, 1922–1934, doi:10.1002/2015JD024203.
Zhou, X., et al. (2011), Nitric acid photolysis on forest canopy surface as a source for tropospheric nitrous acid, *Nat. Geosci.*, *4*(7), 440–443.